# Unveiling micromechanism of Fe minor addition-induced property degradation of an Al-5.1Cu-0.65Mg-0.8Mn (wt%) alloy

Xinjian Chen<sup>a,1</sup>, Bin Wang<sup>a,1</sup>, Zhen Wang<sup>a</sup>, Deyu Zhang<sup>a</sup>, Hong Wang<sup>a</sup>, Jiahai Li<sup>a</sup>, Jin Wu<sup>a</sup>, Junfen Zhao<sup>a</sup>, Xizhou Kai<sup>b</sup>, Manping Liu<sup>b</sup>, Yutao Zhao<sup>b</sup>, Shihao Wang<sup>-c,d</sup>
Shuangbao Wang<sup>a,e,\*</sup>

<sup>a</sup>Yunnan Key Laboratory of Electromagnetic Materials and Devices, National Center for International Research on Photoelectric and Energy Materials, School of Materials and Energy, Yunnan University, Kunming 650500, China

<sup>b</sup>School of Material Science and Engineering, Jiangsu University, Zhenjiang 212013, China

- <sup>c</sup> SuperSTEM Laboratory, SciTech Daresbury Campus, Daresbury WA4 4AD, UK
- <sup>d</sup> School of Chemical and Process Engineering, University of Leeds, Leeds LS2 9JT, UK
- <sup>e</sup> Electron Microscopy Center, Yunnan University, Kunming 650500, China
- \*Contact information: sbwang0617@ynu.edu.cn (S. B. Wang)

#### **Abstract:**

In this paper, the property degradation micromechanism of Al-5.10Cu-0.65Mg-0.8Mn (wt%) alloy induced by 0.5 wt% Fe minor addition was revealed by atomic-scale scanning transmission electron microscopy and energy dispersive X-ray spectroscopy coupled with first-principles calculations. The results show that the Fe minor addition to the Al-Cu-Mg-Mn alloy leads to a slightly decreased Al grain size and formation of coarse Al<sub>7</sub>Cu<sub>2</sub>Fe constituent particles. Fe tends to segregate into the T-phase dispersoids, θ'- and S-phase precipitates by preferentially occupying Cu or Mn sites in these phase structures. The apparent Fe segregation contributes to an increase in stiffness of the T phase and S phase but decreased stiffness of the θ' phase. Formation of the coarse Al<sub>7</sub>Cu<sub>2</sub>Fe constituent particles and decreased stiffness of main precipitates θ' containing Fe result in the degraded strength of the Al-Cu-Mg-Mn-Fe alloy. Further study reveals that corrosion resistance degradation of the Al-Cu-Mg-Mn-Fe alloy is associated with the increased width of precipitation free zones and consecutive grain boundary precipitates. The obtained results have significant implications for the usage of recycled

<sup>&</sup>lt;sup>1</sup>These authors contributed equally to this work.

Al alloys and the potential design strategies of high-performance alloys containing Fe.

*Keywords:* Al-Cu-Mg-Mn alloys; Fe minor addition; Property degradation; Micromechanism; Transmission electron microscopy

#### 1. Introduction

Age-hardening aluminum (Al) alloys are the priority materials for lightweight engineering [1, 2]. 2××× series (Al-Cu-Mg-Mn) alloys achieve a dominant position in aerospace materials due to high specific strength (strength/density) and formability, good heat resistance, and superior damage tolerance [3, 4]. The applications for which such materials are used include the aircraft fuselage and lower wing skin structures. At present, one of the challenges to the sustainability of the Al industry is to increase the usage of recycled material for the sake of energy saving and environmental protection. However, a high content of impurity Fe usually exists in the recycled Al alloys, and it will accumulate during recycling. Normally, the maximum Fe content in the Al-Cu-Mg-Mn alloys is usually limited to 0.15 wt% or less than 0.10 wt% for general purpose use [5]. Therefore, the research focus has been on developing high-performance Al-Cu-Mg-Mn alloys with a high tolerance of Fe content. Understanding the effect of Fe on age-hardening behavior, properties, and associated microstructure is an important way to regulate alloy properties.

In Al-Cu-Mg-Mn alloys, the main alloying element Cu with a maximum solubility of 5.65 wt% in Al forms  $\theta$  (Al<sub>2</sub>Cu) constituent phase during solidification [6]. Another main alloying element Mg with a maximum solubility of ~6 wt% in Al is often used in combination with Cu, forming the S (Al<sub>2</sub>CuMg) constituent phase. Fe is usually considered an impurity elements in Al-Cu-Mg alloys [7]. The extra constituent phases

of Al<sub>7</sub>Cu<sub>2</sub>Fe and Al<sub>6</sub>(Fe,Cu) will form when the content of Fe in Al-Cu-Mg alloys reaches up to 0.1 wt%. The Al<sub>7</sub>Cu<sub>2</sub>Fe and Al<sub>6</sub>(Fe,Cu) constituent phases are generally insoluble during homogenization and solid solution because of the low solubility of Fe (~0.05 wt% at 655 °C) in the Al matrix [8]. In contrast, the θ-Al<sub>2</sub>Cu and S-Al<sub>2</sub>CuMg constituent phases can be dissolved during heat treatment by virtue of the high solubility of Cu and Mg in Al. Normally, the coarse constituent particles with sizes ranging from one to several tens of micrometers are deleterious for the mechanical properties since they are the sources of crack initiation and corrosion without substantial contribution to the yield strength of the alloys.

As an important microalloying element, the Mn addition to Al-Cu-Mg alloys forms rod-like Al<sub>20</sub>Cu<sub>2</sub>Mn<sub>3</sub> (so-called T phase) dispersoids during long-term homogenization, which strongly refine grain size by resistance to recrystallization and grain growth [9, 10]. The thermally stable T-phase dispersoids have sizes in the range of  $0.02-0.5~\mu m$ , which are much smaller than constituent particles [8]. Research has shown that the  $0.4-1.0~\mu m$  Mn added to Al–Cu alloys is able to compensate for the negative effect of Fe because Mn can transfer the Fe-rich constituent particles from the needle-like  $\beta$ -Fe phase to the less harmful Chinese script of  $\alpha$ -Fe (Al<sub>15</sub>(Fe, Mn)<sub>3</sub>(Si, Cu)<sub>2</sub>) [11, 12]. Atomic-scale segregation of Cu at defect sites of the T-phase dispersoids will lead to the preferential dissolution of the adjacent zones inside the particle during corrosion [13]. The S phase with T-phase inclusions is more prone to corrosion than those free of T-phase dispersoids because of the preferential decomposition of Al<sub>20</sub>Cu<sub>2</sub>Mn<sub>3</sub> prior to the S-phase dissolution [14].

In Al-Cu-Mg alloys, decomposition of the supersaturated solid solution (SSSS) during aging treatment results in the formation of hardening nanoprecipitates that are typically metastable and cannot exist outside the Al lattice. For the Al-Cu-Mg alloys with high Mg content, such as the Al-4.57Cu-1.34Mg (wt.%) 2024 alloy, lath-like or rod-like S-phase (Al<sub>2</sub>CuMg) precipitates [15, 16] and one-dimensional (1D) Guinier-Preston–Bagaryatsky (GPB) zones [17, 18] form upon aging. However, plate-like  $\theta'$ phase (Al<sub>2</sub>Cu) precipitates from the Al matrix along with S precipitates and GPB zones during aging of the Al-Cu-Mg alloys with relatively low Mg content, such as the Al-5.10Cu-0.65Mg-0.80Mn (wt.%) alloy investigated in the present study [19-21]. The  $\sigma$ phase (Al<sub>5</sub>Cu<sub>6</sub>Mg<sub>2</sub>, Pm<sub>3</sub>), which forms a thin cubic shape, is an important strengthening precipitate in creep-resistant Al-Cu-Mg-Si/Ag alloys [22, 23]. This phase has also been observed in Si/Ag-free compositions of over-aged Al-4.0Cu-0.3Mg (wt.%) alloy at 200 °C [22]. It is widely known that the formation of coarse Cu-rich Fe-phases and theresulting decrease in the amount of precipitates due to reduced effective Cu content of the alloys available for hardening will lead to reduced ultimate tensile strength and elongation [5, 11]. A Sc-Fe-Si co-segregated θ'-Al<sub>2</sub>Cu/matrix interface by tuning solute repositioning to greatly suppress the coarsening of  $\theta'$  was revealed in an Al-Cu alloy with minor Sc, Fe, and Si addition [24]. Investigation of an Al-Cu-Fe alloy shows that the presence of Mg promotes the formation of S precipitates related to the improvement of high-temperature mechanical properties [25].

Despite these investigations, systematically assessing the effect of Fe microalloying on the microstructure (especially at atomic scale) and properties of Al-

Cu-Mg-Mn alloys is still needed for the development of high-performance Al alloys containing Fe. In the present work, atomic scale high-angle annular dark-filed imaging (HAADF) and energy dispersive X-ray spectroscopy (EDS) in scanning transmission electron microscopy (STEM) and first-principles calculations were coupled to unveil the effect of 0.5 wt% Fe minor addition on the microstructure and mechanical properties of the Al-5.1Cu-0.65Mg-0.8Mn (wt%) alloy. The results show that the Fe minor addition strongly influences the coarse constituent particles, dispersoids and nanoprecipitates of the Al-Cu-Mg-Mn alloy, thereby contributing to the degradation of the mechanical and corrosion properties. The achieved results provide a detailed insight into the interactions among minor Fe and microstructure and properties, which facilitate guidance for the effective utilization of recycled Al alloys

#### 2. Materials and methods

## 2.1 Alloy sample preparation

Two different Al-5.1Cu-0.65Mg-0.8Mn (wt%) alloy ingots with and without 0.50 wt% Fe microalloying were prepared using high-purity (99.99%) aluminum and related master alloys as raw materials. The compositions of alloy ingots analyzed by the titrimetric method are shown in Table 1. Here, two alloys without and with Fe microalloying are abbreviated as AlCuMgMn and AlCuMgMnFe in the context for convenience. The Al alloy ingots were homogenized at 480 °C for 24 h, then subjected to multiple passes of hot rolling at 400 °C with 75% reduction and cold rolling at room temperature with 25% reduction, which finally produced 3 mm-thick alloy plates. Small

pieces of plate samples with the dimension of  $10 \text{ mm} \times 10 \text{ mm} \times 3 \text{ mm}$  by wire cutting were solutionized at  $500 \, ^{\circ}\text{C}$  for  $1 \, \text{h}$  followed by quick water quenching to room temperature. To avoid natural aging, the quenched samples were immediately transferred to an oil bath at  $180 \, ^{\circ}\text{C}$  for artificial aging with a time period of  $0 - 120 \, \text{h}$ .

Table 1 Compositions of the alloys studied (wt%)

Alloys	Cu	Mg	Mn	Fe	Al
AlCuMgMn	5.10	0.65	0.80	0	Bal.
AlCuMgMnFe	5.10	0.65	0.80	0.50	Bal.

#### 2.2 Microstructure characterization

STEM-HAADF observation was carried out using a double aberration-corrected Spectra 300 X-FEG TEM (Thermo Fisher Scientific Inc., USA) operating at 300 kV with a probe convergence angle of 25.2 mrad and a collection angle range of 50 - 200 mrad. To reduce knock-on displacement damage [26] and increase X-ray counts [27], STEM-EDS elemental mappings of the region of interest were acquired by a Super-X G2 detection system attached to the Spectra 300 TEM at a lower acceleration voltage of 200 kV. The samples for STEM observation were prepared in similar ways to those presented in the reference [2].

The size distributions of Al grains in two different peak-aged samples were characterized by a Symmetry electron backscattered diffraction system (EBSD, Oxford Instruments, UK) installed on the Amber scanning electron microscope (SEM, Tescan company, Czech). The samples for EBSD measurements were prepared by

electropolishing using a similar electrolytic solution and temperature to that of twin-jet electropolishing. The morphology and compositions of coarse constituent particles in the samples were respectively characterized with a Gemini SEM500 SEM (ZEISS, Germany) at 5 kV of operating voltage and the attached XFlash 6I100 EDS detector (Bruker, Germany) at 15 kV.

#### 2.3 Property tests

The Vickers hardness of the samples with different aging time was measured by HVS-1000Z hardness tester (Shanghai Zhongyan Inc., China) to evaluate the age-hardening response of two alloy samples. At least ten measurements were conducted to obtain an average hardness value for each aging sample. Room-temperature tensile tests of peak-aged samples with dog-bone shape (2 mm in thickness and 25 mm in gauge length) were carried out at a constant strain rate of 1 mm/min by an AGX-V Electronic Universal Tensile Testing Machine (Shimadzu Inc., Japan). A total of three measurements were used to verify the tensile properties of each sample. The intergranular corrosion (IGC) susceptibility of the peak-aged alloy samples was evaluated by immersion tests with a corrosion solution of 0.33 mol/L H<sub>2</sub>O<sub>2</sub> and 1.0 mol/L NaCl, a corrosion time of 6 h and a constant corrosion temperature of 35 °C.

The electrochemical corrosion behaviors of two peak-aged alloy samples were investigated using the three-electrode system of CHI660E electrochemical workstation (Chenhua instruments, China) with saturated calomel electrode (SCE) as the reference electrode, platinum plate electrode as the auxiliary electrode, and alloy sample (10 mm

× 10 mm ×3 mm in size) as the working electrode. During the electrochemical test, stable open circuit potential (OCP) was confirmed by scanning of 30 min with a drift rate of 1 mV/min and a time per point of 1 s. The electrochemical polarization was tested at a scanning rate of 0.2 mV/s in the range of -1 V to 1 V.

## 2.4 First-principles calculations

First-principles calculations within the density functional theory (DFT) approach were carried out using the Cambridge Serial Total Energy Package (CASTEP) program. The generalized-gradient approximation (GGA) – Perdew-Burke-Ernzerhof (PBE) correlational function and plane—wave ultra-soft pseudo-potentials (USP) were considered during calculations [28]. The formation enthalpies (ΔH) defined in kJ/mol·atom of the atomic models were calculated after geometry optimization [29]. A cutoff of 280 eV for the USP is sufficient to achieve a precision higher than 0.1 kJ mol¹ in the Al-Cu-Mg-Mn-Fe system based on the energy convergence tests. The elastic constants were predicted according to the change in energy induced by applying small elastic strains to the undeformed unit cell lattice with the equilibrium atomic configuration [30-32].

## 3. Results and discussion

## 3.1 Size distribution of Al grains in the alloys

The size distribution of Al gains is one of the important microstructural parameters strengthening Al alloys due to the grain boundary impediment effect on the lattice

dislocation [33]. For that reason, EBSD experiments were conducted on the peak-aged AlCuMgMn and AlCuMgMnFe alloys to characterize the size difference of Al grains induced by the micro-addition of Fe. Fig. 1a shows a representative inverse pole figure (IPF) map of the AlCuMgMn alloy. Colour code representing different crystal orientations of Al grains is shown in the inset of Fig. 1a. Apparently, the peak-aged AlCuMgMn alloy displays fully recrystallized and randomly oriented Al grains. The corresponding statistical result shows that the average grain size (d) of Al is ~35  $\mu$ m, as shown in Fig. 1b.

Figs. 1c and d show representative IPF maps and corresponding size distribution of Al grains in the peak-aged AlCuMgMnFe alloy, respectively. Similar to the AlCuMgMn alloy, the AlCuMgMnFe alloy is also composed of fully recrystallized and randomly oriented Al grains (Fig. 1c and inset). However, the Al grain size of AlCuMgMnFe alloy is universally smaller than that of AlCuMgMn alloy. Specifically, the average Al grain size of AlCuMgMnFe alloy is estimated to be ~30 μm on the basis of statistical measurements (Fig. 1d). Therefore, the micro-addition of 0.5wt% Fe has a potential effect of refining the Al grains of the AlCuMgMn alloy. Identically, results by Zhao et al. in a study of Al-Cu alloy with small Fe addition also indicate that higher Fe content results in a smaller Al grain size [25]. Studying the effect of 0.3wt% Sc-0.2wt% Fe coaddition on the grain structures of Al-2.5wt% Cu alloy, Gao et al. also found the reduced Al grain size of the Al-Cu-Sc-Fe alloy compared to that of Al-Cu alloy [34]. They also suggested that the presence of minor Fe is in favor of eliminating (Cu, Sc)-rich W-phases in the Al-Cu-Sc alloy and promoting Al<sub>3</sub>Sc precipitation during

homogenization.

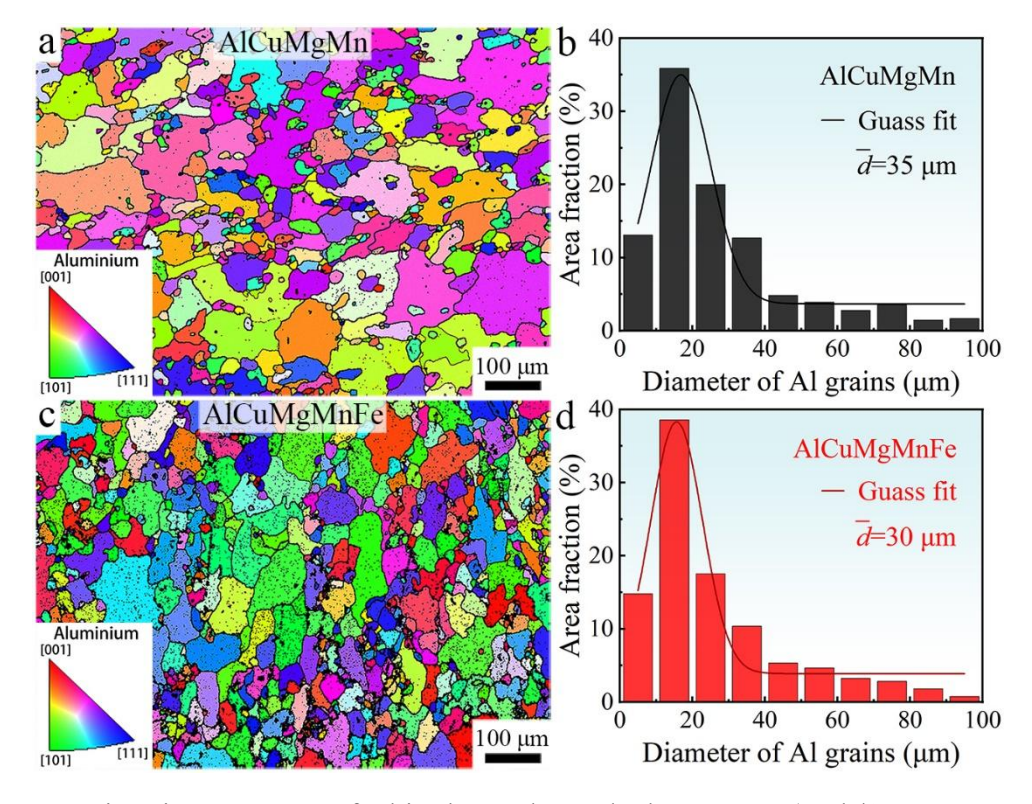


Fig. 1. Grain microstructure of Al in the peak-aged AlCuMgMn (88 h/180 °C, a and b) and AlCuMgMnFe (64 h/180 °C, c and d) alloys. (a) and (c) are the representative IPF maps collected using EBSD, and (b) and (d) are the corresponding statistical grain size distributions. Stereographic triangles given in the insets of (a) and (c) are the corresponding colour code for the IPF maps.

## 3.2 Coarse constituent particles

The constituent phases (or intermetallic particles), which are nominally larger than 1 µm in size, normally have an adverse effect on the mechanical properties due to their potential sites as sources of crack initiation, crack growth, and localized corrosion without significantly enhancing the yield strength of the alloys [8, 35]. It is, therefore, essential to study the effect of Fe microalloying on the constituent phases of

AlCuMgMn alloy. In the peak-aged AlCuMgMn alloy, some coarse constituent particles with a size of around 3.4  $\mu$ m are observed inside the Al matrix (Fig. 2a). The number density of constituent particles is measured to be 778/mm². The area shown in (a) was further probed by SEM-EDS mapping with elemental maps shown for Al, Cu, Mg, Mn, and Fe (Figs. 2b-f). In the case of Fe, Mn-containing Al-Cu-Mg alloys, it has also been reported that typical constituent particles include Al<sub>2</sub>Cu, Al<sub>2</sub>CuMg, Al<sub>6</sub>Mn, Al<sub>7</sub>Cu<sub>2</sub>Fe and  $\alpha$ -Fe [8, 25, 36, 37]. According to the EDS elemental mapping analyses, it can be found that the constituent particles in the peak-aged AlCuMgMn alloy consist mainly of Al<sub>2</sub>Cu particles with a small amount of  $\alpha$ -Fe and Cu-containing Al<sub>6</sub>Mn and Al<sub>2</sub>CuMg. Here, it should be mentioned that the formation of  $\alpha$ -Fe is associated with the Fe impurity remaining in the master alloys used for the melting of alloys. Fig. 2g and inset provide the EDS spectrum of the elemental mappings and corresponding chemical composition, respectively, demonstrating a very small amount of Fe in the AlCuMgMn alloy.

In the case of peak-aged AlCuMgMnFe alloy, there are increased size (~4.8 μm) and number density (1334/mm²) of coarse constituent particles as compared to those of AlCuMgMn alloy, as shown in Fig. 2h. Figs. 2i-m show the EDS elemental mappings of Al, Cu, Mg, Mn, and Fe, respectively. Detailed analyses indicate that the constituent particles are mainly composed of Al<sub>7</sub>Cu<sub>2</sub>Fe containing Mn. It has also been reported that Mn may substitute for Fe in some constituents [38, 39]. Additionally, a small proportion of Al<sub>6</sub>(Mn, Fe) can be found in the alloys. Fig. 2n and inset show the EDS spectrum of the elemental mappings and corresponding chemical composition,

respectively, both of which confirm the existence of Fe in the studied AlCuMgMnFe alloy. In brief, it can be concluded that 0.5wt% Fe microalloying of the AlCuMgMn alloy helps transform the Al<sub>2</sub>Cu constituent particles into Mn-containing Al<sub>7</sub>Cu<sub>2</sub>Fe constituent particles with increased size and number density.

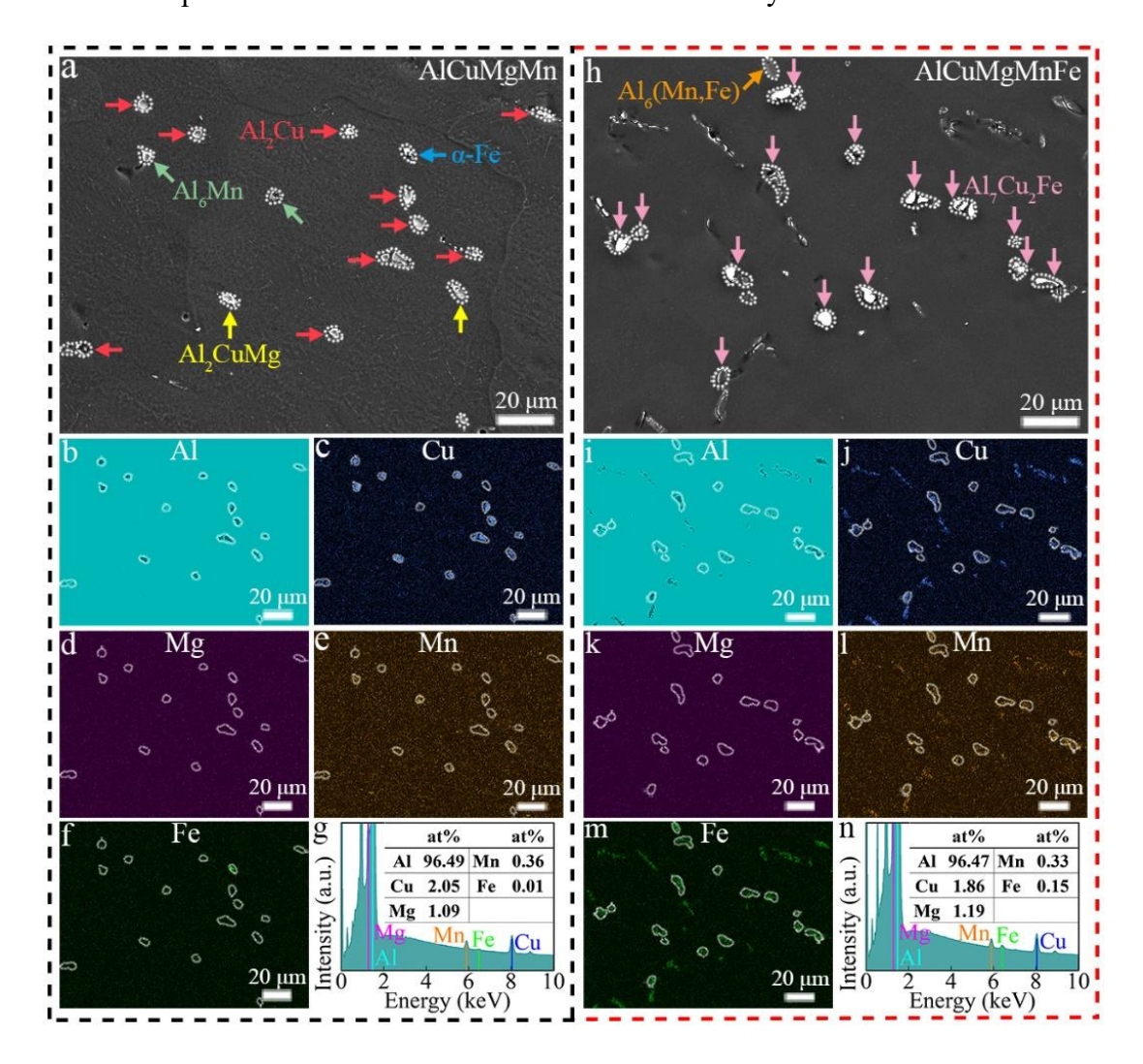


Fig. 2. SEM-EDS mapping analyses of coarse constituent particles in the peak-aged AlCuMgMn alloy (a-g) and AlCuMgMnFe alloy (h-n), showing the changes in phase types, shape, size and N<sub>A</sub> after Fe microalloying. (a) and (h) SEM images. (b-f) and (i-m) EDS mappings of the areas shown in (a) and (h), respectively. (g) and (n) EDS spectra and corresponding element contents (insets) collected at the areas shown in (a) and (h), respectively.

# 3.3 Compositional characteristics of dispersoids and nanoprecipitates

In addition to the micrometer-size constituent particles, the effect of minor Fe on the hardening particles at the nanometer scale in two different peak-aged alloys was also evaluated by HAADF-STEM images, as shown in Fig. 3. Atomcially resolved HAADF image shows that five types of nano-size particles exist in the peak-aged AlCuMgMn alloy, namely plate-like  $\theta'$ -phase precipitates (Fig. 3a), lath-like S precipitates (Fig. 3b), cubic  $\sigma$  precipitates (Fig. 3c), needle-like GPB zones (Fig. 3c) and T-phase dispersoids (Fig. 3d). High-magnification HAADF image (Fig. 3e) shows that two ends of one S-phase precipitate are connected with two isolated  $\theta'$ -phase precipitates. Strong strain fields in the front of two ends of the S-phase precipitate trigger  $\theta'$  precipitates to nucleate, forming an interconnected  $\theta'$ -S complex [16, 19]. Besides the  $\theta'$ -S complex, the densely distributed GPB zones with a truncation size of several nanometers are distinguishable in the alloy.

Fig. 3f is a low-magnification HAADF image overviewing the major microstructure of nano-size hardening particles. The nano-particles are distinct according to their size, morphology, and orientation. Rather obviously, many rod-like T-phase dispersoids with an average diameter of  $\sim$ 120 nm and average length of  $\sim$ 290 nm exist within the Al matrix. Besides, much finer  $\theta'$ - and S-phase itprecipitates form in between the T-phase dispersoids. Of note is that the amount of the  $\theta'$  precipitates is dominant over that of the S-phase precipitates within the same observation area. Most S-phase precipitates coexist with  $\theta'$  precipitates in the manner of  $\theta'$ -S complex. The

observation result also indicates that the amount of the  $\sigma$ -phase precipitates is significantly lower compared to other nano-size particles in the peak-aged AlCuMgMn alloy. The possible reason is that the  $\sigma$ -phase precipitates are only easy to form in the over-aged Al-Cu-Mg alloys under high-temperature ( $\geq 200$  °C) aging [22]. The present observed nanoprecipitates in the peak-aged AlCuMgMn alloy are generally consistent with previous experimental observations in similar alloy samples [19].

Similar to the peak-aged AlCuMgMn alloy, the  $\theta'$ -phase precipitates (Fig. 3g), Sθ' complex (Fig. 3h), σ-phase precipitates (Fig. 3i), GPB zones (inset in Fig. 3i) and Tphase dispersoids (Fig. 3j) are also identified to coexist in the peak-aged AlCuMgMnFe alloy. Other additional nano-size particles are not identified in the peak-aged AlCuMgMnFe alloy. A low-magnification HAADF image (Fig. 3k) and careful measurement indicate that these nano-size particles maintain identical shape, size, and distribution to those in the peak-aged AlCuMgMn alloy. In view of the above observations, it is concluded that the 0.5wt% Fe microalloying of the AlCuMgMn alloy does not evidently affect the configurations of T-phase dispersoids and peak-aged nanoprecipitates. The currently observed Fe effect is contrary to other microalloying elements such as Si, Cd, Ag, and Sc, which produce a significant influence on the precipitate microstructure in the peak-aged Al-Cu-Mg alloys [2, 19, 40-42]. For example, Han et al. observed that the addition of Sc can significantly suppress the formation of the peak-aged  $\theta$ '- and S-phase precipitates but help stabilize the GPB zones during aging at 180 °C [19]. The insufficient vacancies and dragging effect of Sc to Cu in the Al-Cu-Mg-Sc alloy are expected to be the reason for the Sc-modified precipitate

microstructure during thermal aging.

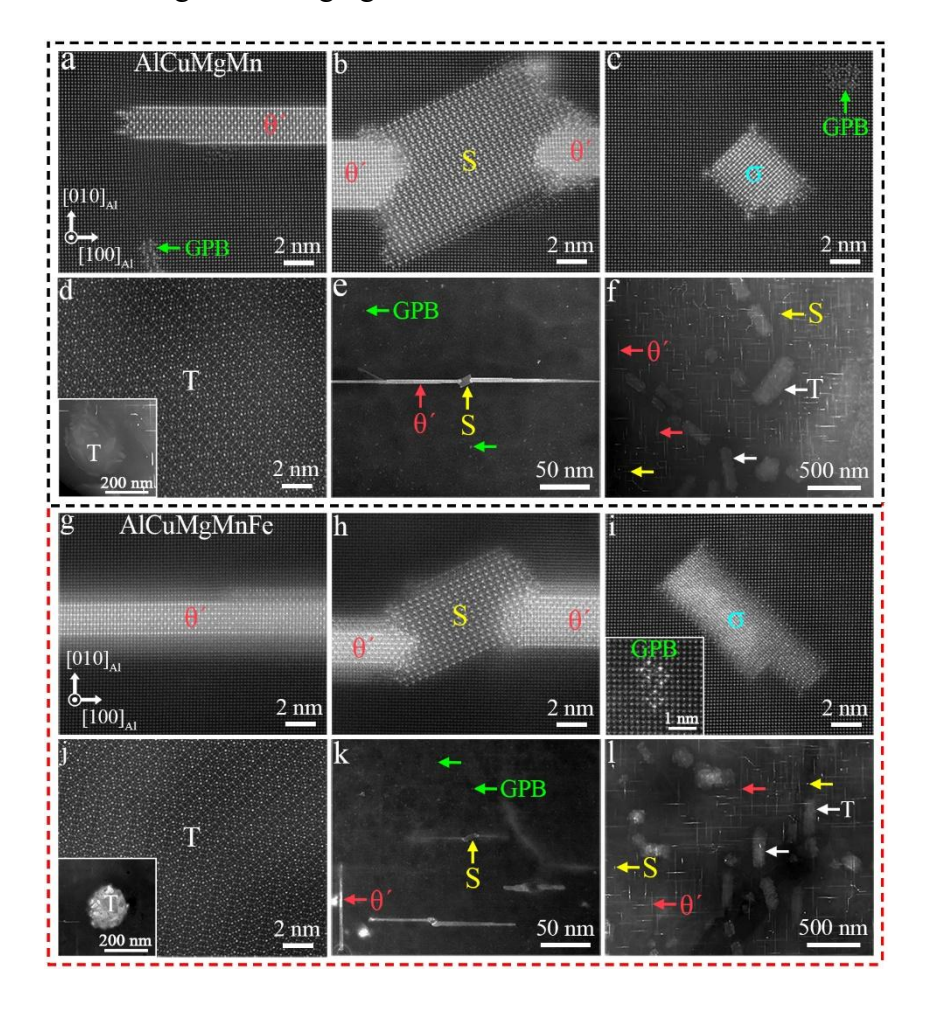


Fig. 3. HAADF images of nano-size particles in the peak-aged AlCuMgMn (a-f) and AlCuMgMnFe (g-l) alloys. (a, g), (b, h), (c, i) and (d, j) Atomic-scale  $\theta'$  precipitates,  $\theta'$ -S complex,  $\sigma$  precipitates and T-phase dispersoids, respectively. Insets in (d) and (j) are corresponding morphology. Inset in (i) is atomic-scale GPB zone. (e and k) High-magnification images showing the coexistence of  $\theta'$ -S complex and GPB zones. (f and l) Low-magnification images showing the overviews of nano-size particles.

The characteristics of T-phase (Al<sub>20</sub>Cu<sub>2</sub>Mn<sub>3</sub>) dispersoids in the peak-aged Al-Cu-Mg-Fe alloy were analyzed using STEM-HAADF and -EDS elemental mapping, as shown in Fig. 4. Fig. 4a shows a high-magnification HAADF image of a rod-shape T-

phase dispersoid viewed end-on. Figs. 4b-f show the corresponding EDS elemental mappings of Al, Cu, Mg, Mn and Fe. It is noted that the T-phase dispersoid is rich in Mg and Fe in addition to the nominal Al, Cu, and Mn. Fig. 4g shows the corresponding EDS spectrum of the elemental mappings, demonstrating the Fe enrichment in the T-phase dispersoid. Atomic-scale HAADF observation reveals that the rod-phase T-phase dispersoid is decorated by S-phase precipitates at prior T-Al interfaces, as shown in Fig. 4h. This explains that there are apparent Mg signals in the T-phase dispersoids shown in Fig. 4d. Unlike the S-phase precipitates, no θ'-phase precipitates are detected at the T-Al interface. It is well known that the T-phase dispersoids usually form during homogenization. During subsequent artificial aging, the S precipitates were prone to nucleate at T/Al interfaces with specific orientation relationships [43, 44]. In comparison with the S phases normally precipitated from the Al matrix, it is more difficult for the segregated S precipitates at T/Al interfaces to coarsen during over-aging due to the depleted Cu and Mg solutes in the surrounding matrix by S precipitation.

Fig. 4i shows another high-magnification HAADF image of a rod-shaped T-phase dispersoid viewed side-on. As expected, many S-phase precipitates are clearly observed to be decorated around the T-phase dispersoids. Figs. 4j-n portrays the corresponding elemental distributions of (i), from which one can see that the T-phase dispersoid is mainly composed of Al, Cu, and Mn. In addition, it was found that the adhered nanoparticles consist of Al, Cu, and Mg, which fall in line with the composition of S-phase precipitates. Consistently, there is an apparent Fe distribution (Fig. 4n) at the T-phase area in addition to the Al, Cu, and Mn. Fig. 4o shows EDS spectrum

corresponding to the elemental mappings, where the characteristic Fe peak visible in addition to the peaks of Al, Cu, Mg, and Mn, again demonstrates the Fe enrichment in the T-phase particle. Fig. 4p displays the schematic of the T-/S-phase aggregates on the basis of the above observation, where apparent Fe enrichment is found in the T-phase dispersoids. As far as we are aware, there have been few reports to date on the Fe-enriched T-phase dispersoids, which is crucial to deepen the understanding of Fe microalloying for Al alloy applications.

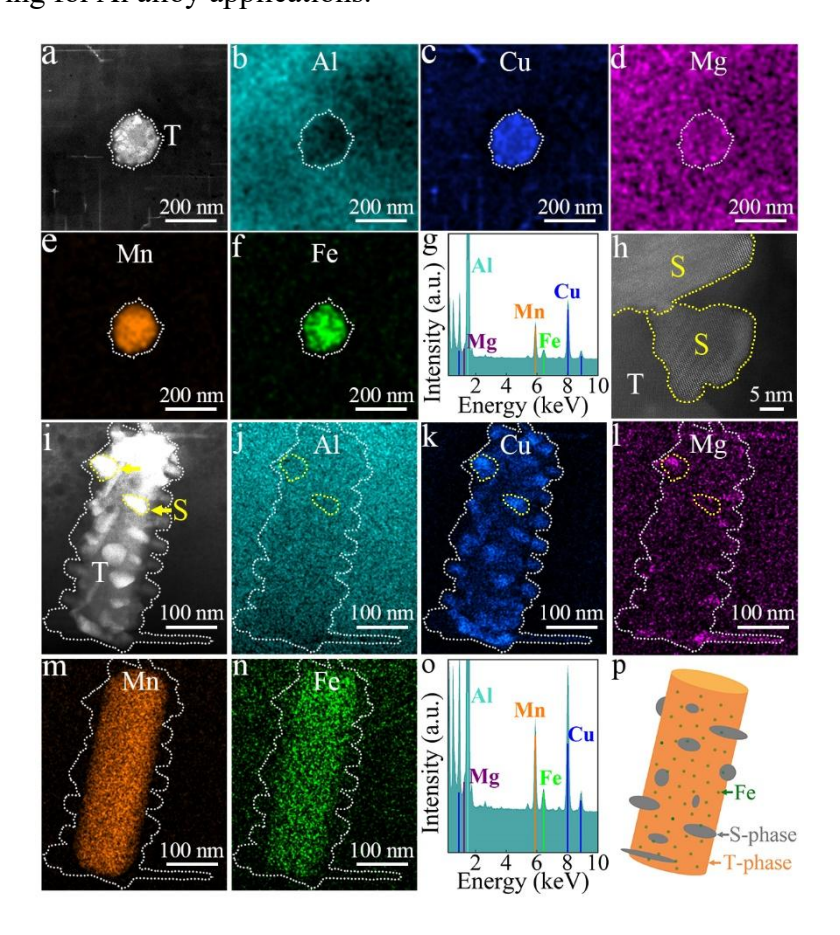


Fig. 4. Feature of T-phase dispersoids in the peak-aged AlCuMgMnFe alloy. (a - h) HAADF image of a T-phase dispersoid viewed end-on, corresponding EDS mappings, EDS spectrum and atomic-resolution HAADF image of S-phase precipitates around the T-phase dispersoids. (i - o) HAADF image of a side-on T-phase dispersoid decorated with some S-phase precipitates, corresponding EDS mappings and EDS spectrum. (p)

Schematic of the Fe-rich T-phase dispersoids decorating with S-phase precipitates.

To further identify the specific occupation of Fe in the T-phase dispersoids, atomically resolved EDS elemental mappings were operated at a low accelerating voltage of 200 kV. In practice, it is difficult for us to obtain the clear elemental mappings of [010]-oriented T-phase dispersoids at the atomic scale due to serious knock-on displacement damage during long-time EDS signal collection. In contrast, the structure damage was alleviated for the T-phase dispersoids along [101] at the same acquisition conditions. The possible reason is that more channels exist in the T-phase atomic structure along [101] orientation compared to [010] orientation, reducing the probability of interaction between the electron beam and the atoms in the sample.

Fig. 5a shows the clear atomic structure of a [101]-oriented T-phase dispersoid formed in the peak-aged AlCuMgMnFe alloy, from which one can see a similar atomic configuration of the T-phase with previous report [9]. Figs. 5b-f are the atomic-resolution EDS mappings of Al, Cu, Mg, Mn, and Fe, respectively, showing that the T phase is rich in Al, Cu, and Mn but deficient in Mg. Also, it is easy to find some discrete dots associating with Fe signals inside the structure (Fig. 5f), which demonstrate Fe occupation at some special sites of the structure. The superimposed Cu map and HAADF image (Fig. 5g) show that the brightest dots in the HAADF image correspond to Cu sites. Other atomic columns at the perimeter of Cu sites are associated with Mn or Mn/Cu mixture. The displayed superposition of the Fe map, Mn map and HAADF image (Fig. 5h) directly signifies the partial Fe occupation at the original Cu or Mn sites.

It is reasonable to observe the bright contrast at the Cu sites replaced by partial Fe in the HAADF image due to larger atomic number of Fe than those of Al and Mn. Fig. 5i shows an EDS spectrum acquired from the area shown in the HAADF image. The quantified EDS spectrum shows that the content of Fe in the T-phase dispersoid can reach up to 1.01 at.%, further verifying the existence of Fe in the T-phase dispersoids in addition to the Al, Cu, and Mn.

The first principles formation enthalpies were then calculated to check the different Fe occupations in the T-phase structures suggested by atomic resolution EDS elemental mappings, as shown in Fig. 5j. Calculation results show that the pure T-phase structure has a  $\Delta H$  of -25.5 kJ/mol atom. In the case of the Cu replaced with Fe, two inequivalent positions of Cu respectively occupied by Fe in the structure were considered. Models T-Cu(1)<sub>Fe</sub> and T-Cu(2)<sub>Fe</sub> have relatively lower  $\Delta H$  of -31.5 kJ/mol·atom and -33.8 kJ/mol·atom, respectively, which indicate that the Cu sites (partially) replaced with Fe in T-phase structure is energetically favourable. In the case of the Mn replaced with Fe, three unequivalent Mn positions respectively occupied by Fe in the structure were constructed. The  $\Delta H$  of -26.2 kJ/mol·atom, -27.1 kJ/mol·atom and -27.4 kJ/mol·atom were identified for the models T-Mn(1)<sub>Fe</sub>, T-Mn(2)<sub>Fe</sub> and T-Mn(3)<sub>Fe</sub>, respectively. These three different models exhibit lower  $\Delta H$  than the pure Tphase structure, implying an energetically favorable process for the Mn sites replaced with Fe in the structure. Similar to early works [5, 12, 25], the Fe atoms are prone to replace the Mn atoms of the Mn-bearing phases in the Fe-containing Al-Cu-Mg-Mn alloys. In short, the present calculation results well support the Fe enrichment in the T- phase dispersoids identified by EDS elemental mapping analysis.

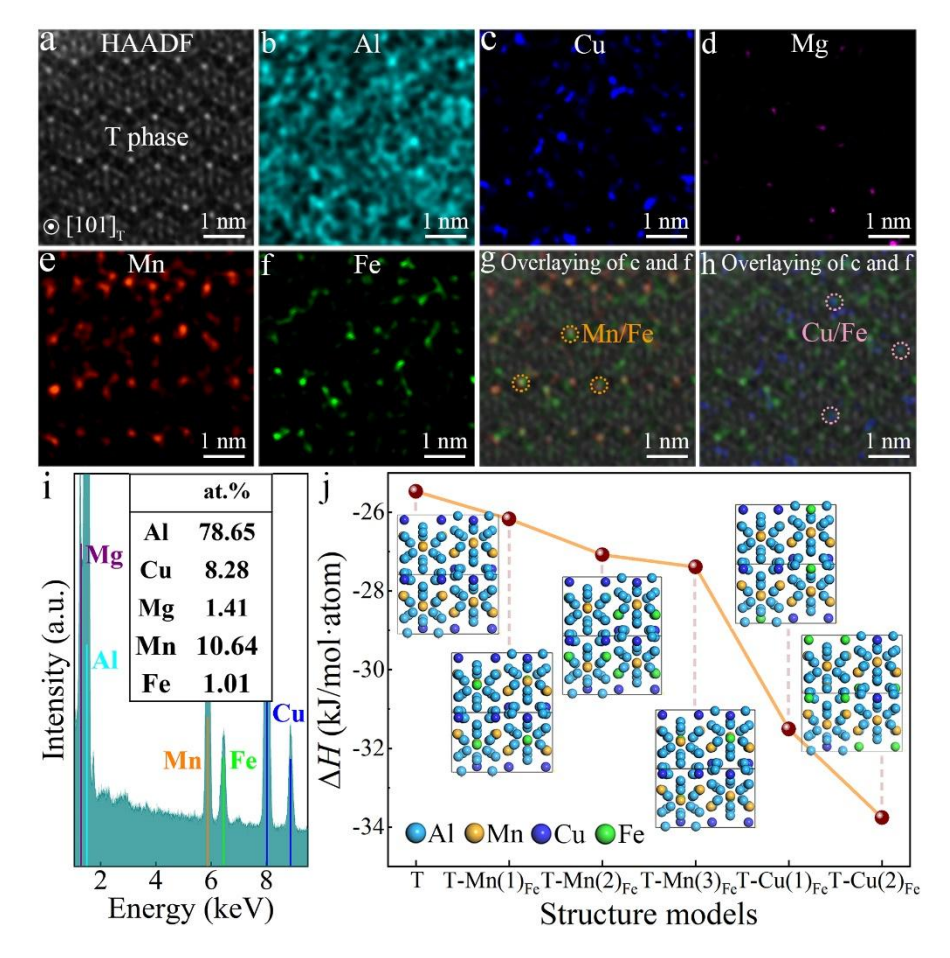


Fig. 5. Atomic-resolution STEM-EDS mappings of one [101]-oriented T-phase dispersoid and energy calculations of several Fe-modified structure models of T phase along [010]. (a - i) HAADF image, corresponding elemental maps, superimposed map of Mn and Fe showing the Fe occupation at Mn sites in the T-phase structure, superimposed map of Cu and Fe showing Fe occupation at Cu, and EDS spectrum. (j)  $\Delta H$  of the T-phase with Cu and Mn sites substituted by Fe atoms.

In addition to the T-phase dispersoids, composition characteristics of two principle strengthening precipitates of  $\theta'$  and S in the peak-aged AlCuMgMnFe alloy were also examined by the atomic scale STEM-EDS and first principles energy calculations. The  $\theta'$  precipitates were first analyzed, as shown in Fig. 6. Fig. 6a shows an atomic-

resolution HAADF image of a mature  $\theta'$  precipitate, which is featured with rhombic Cu lattice when viewed along the  $[100]_{\theta'}$  direction. Figs. 6b-d present EDS mappings of the elements Al, Cu, and Fe from the area shown in (a). It is seen that the  $\theta'$  precipitate is mainly composed of Al and Cu (Figs. 6b and c). Interestingly, some sparse Fe occupations are also observed in the  $\theta'$  (Fig. 6d), which is different from the apparent Fe enrichment in the T-phase dispersoids shown in Fig. 5. Superimposed HAADF image and Cu map clearly shows the brightest dots in the HAADF image belong to Cu occupation, as shown in Fig. 6e. Further occupation analysis from the superimposed HAADF image and Fe map gives that the Fe could occupy at the original Cu sites in the  $\theta'$  structure, as shown in Fig. 6f. Fig. 6g shows a EDS spectrum corresponding to the EDS mapping area, in which a weak Fe peak is visible among the peaks of Al, Cu, and Mg. The quantified result of the EDS spectrum shows that there is a very low Fe content of around 0.10 at.% in the  $\theta'$  precipitates.

The unusual Fe dopping at original Cu sites of the above-observed  $\theta'$  precipitates was then explained by the formation enthalpy calculations with supercells of  $1\times1\times2$   $\theta'$  unit cells. Fig. 6h shows the  $\Delta H$  as a function of different ratios of Cu substituted by Fe in the  $\theta'$ -phase model (termed as  $\theta'$ -xCu<sub>Fe</sub> in the following text). The  $\Delta H$  of  $\theta'$  phase structure is calculated to be -20.9 kJ/mol·atom, which shows a good agreement with the value -17.4 kJ/mol·atom from the reference [45]. The  $\theta'$  structure show a rapid  $\Delta H$  decrease with the increase of the Cu<sub>Fe</sub> ratio to 50% and afterwards, the  $\Delta H$  remains almost unchanged when the Cu<sub>Fe</sub> ratio reaches 75%. The decreased  $\Delta H$  of  $\theta'$  structure as substitution ratio of Cu<sub>Fe</sub> increases before 75% indicates that the partial substitution

of Cu in  $\theta'$  by Fe is energetically favourable, thus a spontaneous process during thermal aging.

Similarly, substituting Au for Cu in  $\theta'$  also contributes to an almost linear decrease of  $\Delta H$  with the amount of Au addition to  $\theta'$  [45]. However, the  $\Delta H$  of  $\theta'$ -xCu<sub>Fe</sub> increases during substitution ratios ranging from 75% to 100%. This indicates high-ratio Cu substitution by Fe is energetically forbidden, which well explains the full occupation of Fe at only several Cu sites in the  $\theta'$  revealed by the Fe mapping shown in Fig. 6h. As far as we know, there is currently limited research on the role of Fe atoms in  $\theta'$ .

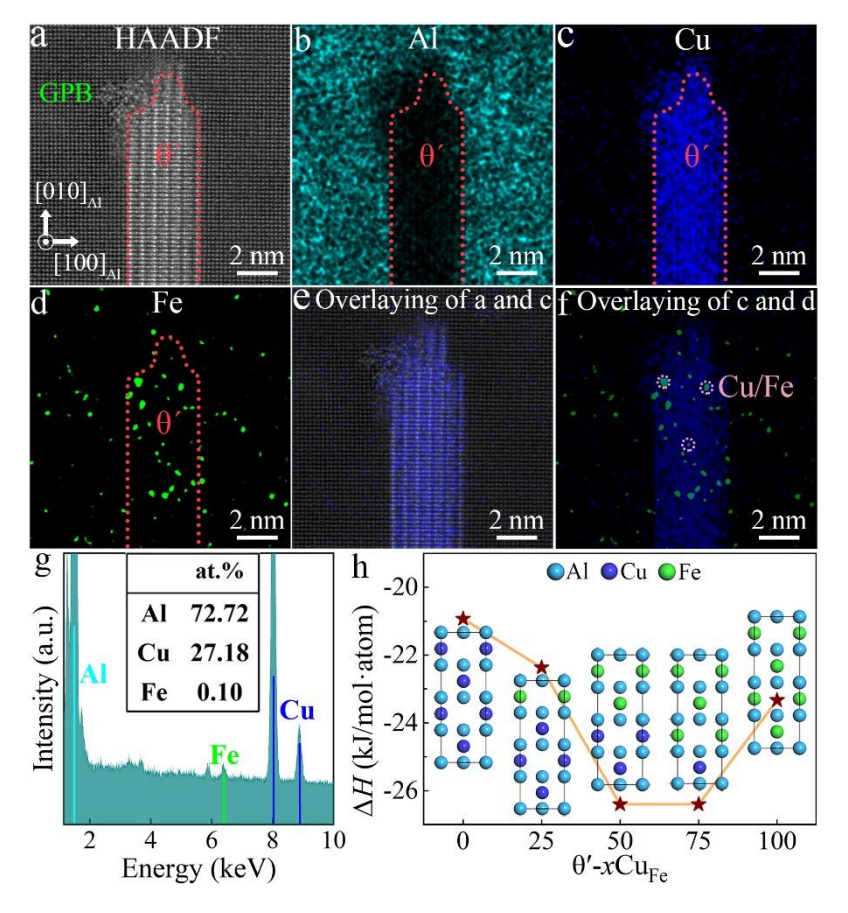


Fig. 6. STEM-EDS analysis of a θ' precipitate in the peak-aged AlCuMgMnFe alloy. (a) Atomic resolution HAADF image. (b - d) Corresponding EDS mappings of Al, Cu, and Fe. (e) Superimposed map of (a) and (c), showing that the brightest dots in the HAADF images are primarily composed of Cu. (g) Superimposed map of (a) and (f),

highlighting that Fe fully occupies the some Cu sites in the  $\theta'$ . (i) EDS spectrum of the area in (a). (j)  $\Delta H$  of the  $\theta'$  structures with different substitution ratios of Cu<sub>Fe</sub>.

Next, the composition characteristics of S precipitates in the AlCuMgMnFe alloy were also analyzed by atomic-resolution STEM-EDS elemental mapping and first principles energy calculations, as shown in Fig. 7. Fig. 7a shows an atomic-resolution HAADF image of two rod-shape S-phase precipitates in contact with one end of platelike  $\theta'$  precipitates in the peak-aged AlCuMgMnFe alloy. Figs. 7b-e show the corresponding elemental mappings of Al, Cu, Mg and Fe, respectively. It is seen that Al, Cu, and Mg elements are uniformly distributed throughout the S precipitates. However, a clear signal of Fe can be found in the Fe mappings, which implies the Fe enrichment in the S precipitates (Fig. 7e). Fig. 7f is the superimposed image of the HAADF image (a) and Cu elemental mapping (c), showing the primary Cu occupation at the brightest sites in the HAADF image of S precipitates. The superimposed image of Cu elemental mapping (c) and Fe elemental mapping (e) suggests the partial Cu sites occupied by Fe atoms in the S-phase structure, as shown in Fig. 7g. Similarly, Sha et al. found that there is also a preferential substitution for original Cu sites by Si in the Sphase precipitates in the peak-aged 2024 alloy by atomic probe technology [46]. Fig. 7h provides a corresponding EDS spectrum line of elemental mappings in which a weak characteristic peak of Fe is identified. The quantified analysis shows that the Fe concentration in the peak-aged S precipitates is around 0.13 at.%, as shown in the inset of Fig. 7h. It is worth noting that the simultaneously acquired EDS elemental mappings

of the  $\theta'$  precipitate contacted with S-phase precipitate are also found to have Fe doping, which is consistent with the observation from Fig. 6.

To further substantiate the enrichment of Fe in the S-phase precipitates, the Fe concentration of the S-phase precipitates in the largely overaged (120 h of aging) AlCuMgMnFe alloy was analyzed again using STEM-EDS, as shown in Figs. 7i-n. Fig. 7i shows an atomic-resolution HAADF image of S-phase precipitates and Figs. 7j – m are corresponding elemental mappings of Al, Cu, Mg, and Fe. Similar to the peak-aged S-phase precipitates, the overaged S-phase precipitates also contain a certain amount of Fe, as shown in Figs. 7m and n. Detailed analyses indicate that the over-aged S-phase precipitate has a concentration of 0.21 at.% (inset in Fig. 7n), which is higher than that of peak-aged S precipitate. In other words, there is a continuous increase in Fe content inside the S-phase precipitate with the prolongation of aging time.

Fig. 7g clearly shows that the Cu sites in the S-phase precipitates tend to be replaced with Fe, forming Fe-containing S precipitates during aging. Hence, the first-principles energy calculations were conducted on the S phase with different Cu content substituted by Fe, as shown in Fig. 7o. Regarding the pure S-phase structure without Fe occupation, the calculated  $\Delta H$  is -20.7 kJ/mol·atom, which lies within previous study [47]. The  $\Delta H$  decreases progressively with the gradual substitution of Cu by Fe, from initial -20.7 kJ/mol·atom of pure S phase to -22.4 kJ/mol·atom of S-0.8CuFe structure. The  $\Delta H$  decreases a lot to -24.7 kJ/mol·atom as full substitution of Cu by Fe occurs in the S-phase structure. This finding strongly suggests that the Cu atoms inside S-phase precipitates can be substituted with Fe atoms. Also, the more Fe replaces Cu in the S

structure, the more favorable the energy is. In practice, it is difficult to observe 100% substitution of Cu by Fe in S-phase precipitates due to the limited diffusion rate and concentration of Fe atom in the Al matrix.

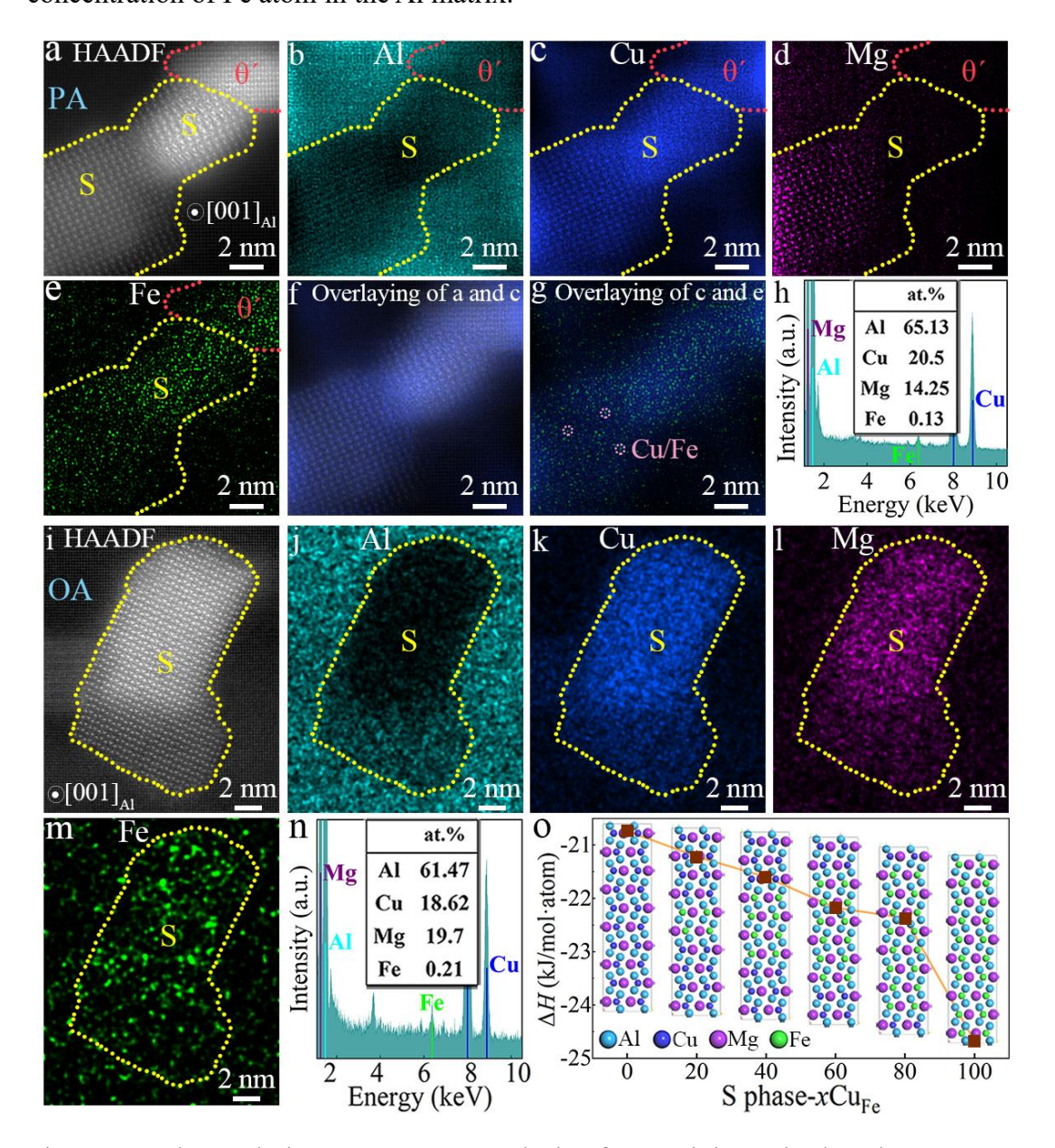


Fig. 7. Atomic-resolution STEM-EDS analysis of S precipitates in the AlCuMgMnFe alloy and energy calculations. (a - i) HAADF image of a peak-aged S precipitate, corresponding EDS elemental mappings of Al, Cu, Mg and Fe, superimposed image of (a) and (c), superimposed image of (a) and (f) and EDS spectrum, respectively. (j)  $\Delta H$  of the S-phase structures with different substitution ratios of  $Cu_{Fe}$ . (k - p) HAADF

image of an over-aged S precipitate, corresponding EDS elemental mappings of Al, Cu, Mg and Fe, and EDS spectrum, respectively.

## 3.4 Mechanical properties of relevant Fe-containing phases

The STEM-EDS at atomic scale and first principles energy calculations presented above have unambiguously demonstrated the Fe-containing secondary phases in the AlCuMgMnFe alloy. It is known that the secondary phases play a crucial role in the total strengthening of Al alloys; the mechanical properties of Fe-containing T-phase dispersoids,  $\theta'$ - and S-phase precipitates are therefore predicted by the first-principles calculations of elastic constants. Table 2 summaries the elastic constants of T-,  $\theta'$ - and S-phase structures and their corresponding Fe-modified structures. The key mechanical parameters of bulk modulus (B), shear modulus (G) and Young's modulus (E) for their different phase structures can be achieved on the basis of the known elastic constants, as shown in Fig. 8.

Table 2 Elastic constants of relevant phases in the alloys (unit: GPa)

Configuration	$C_{11}$	$C_{12}$	$C_{13}$	$C_{22}$	$C_{23}$	$C_{33}$	C <sub>44</sub>	$C_{55}$	$C_{66}$
T phase	166	63	52	185	62	179	26	43	55
T-Cu(2) <sub>Fe</sub>	219	50	63	215	53	222	33	79	50
T-Mn(3) <sub>Fe</sub>	161	74	56	177	75	165	34	52	57
S phase	123	67	43	115	42	153	27	71	31
S-100Cu <sub>Fe</sub>	94	53	73	134	55	139	53	87	78

θ' phase	210	37	58	 	179	82	 45
$\theta$ '-75Cu <sub>Fe</sub>	165	75	63	 	145	51	 58

The T-phase structure yields the values of 98 GPa, 48 GPa, 0.490, and 124 GPa for the B, G, G/B, and E, respectively. For the substituted Cu (by Fe) case, the stable T-Cu(2)<sub>Fe</sub> structure has higher B (110 GPa), G (65 GPa), G/B (0.591), and E (163 GPa). Whereas for the substituted Mn (by Fe) case, the stable T-Mn(3)<sub>Fe</sub> structure has almost similar B (101 GPa), G (48 GPa), G/B (0.475) and E (125 GPa) with T-phase structure. It is important to note that the first-principles calculations for the substituted Mn case (by Fe) are not much different from those for the T-phase, so we mainly focus on the case of substituted Cu (by Fe). The higher the G/B value is, the more brittle the structure behaves, considering that the B and G are respectively associated with the materials' fracture and plastic deformation. This means that the T-phase will become brittle after Fe segregation occurs. In addition, larger E value of Fe-containing T-phase indicates higher stiffness than that of pure T-phase.

In the case of the S phase, it is found that the Fe-containing S-100Cu<sub>Fe</sub> structure has higher B (81 GPa), G (56 GPa), G/B (0.691), and E (137 GPa) than the pure S-phase structure. That is to say, the S-phase exhibits reduced ductility but increased stiffness after being substituted by Fe, allogenous to the T-phase structure. Conversely, relatively low B (98 GPa), G (50 GPa), G/B (0.510), and E (128 GPa) are observed for the  $\theta'$ -75Cu<sub>Fe</sub> structure compared with those of the pure  $\theta'$  structure. This means that the ductility of the  $\theta'$ -phase is increased, but the stiffness is decreased after the substitution

of Fe, in contrast to the decrease in ductility of the S-and T-phases after being substituted by Fe.

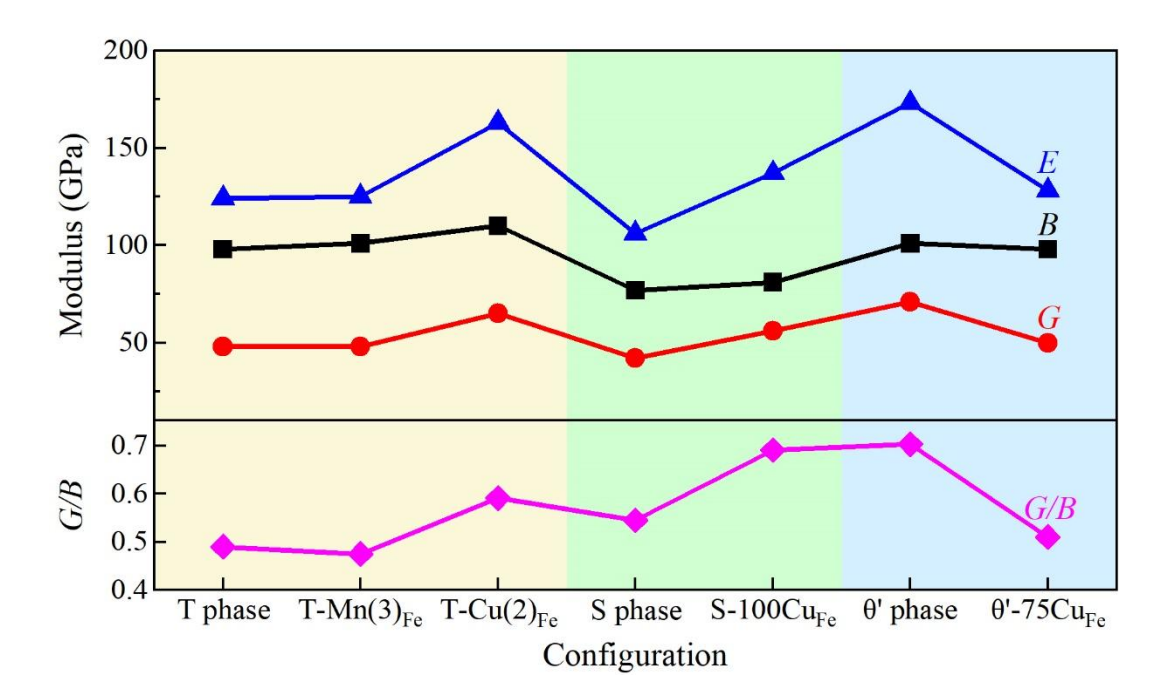


Fig. 8. Calculated mechanical parameters, i.e., bulk modulus B, shear modulus G, Young's modulus E and G/B ratio of the relevant phases in the alloys.

The mechanical stability of the Fe-containing T-,  $\theta'$ - and S-phases were further evaluated using Born's criteria. For an orthorhombic crystal system (T- and S-phases), the Born criterion of mechanical stabilities are [48]

$$C_{11} > 0; C_{22} > 0; C_{33} > 0; C_{44} > 0; C_{55} > 0; C_{66} > 0$$

$$C_{11} + C_{22} + C_{33} + 2(C_{12} + C_{13} + C_{23}) > 0$$

$$C_{11} + C_{22} - 2C_{12} > 0$$

$$C_{11} + C_{33} - 2C_{13} > 0$$

$$C_{22} + C_{33} - 2C_{23} > 0.$$

For a tetragonal crystal system ( $\theta'$  phase), the Born criterion of mechanical stabilities are [49]

$$C_{11} > |C_{12}|$$

$$C_{33}(C_{11} + C_{12}) > 2(C_{13})^2$$

$$C_{44} > 0$$

$$C_{66} > 0$$
.

From our calculated elastic constants as listed in Table 2, the above Born criteria of the mechanical stable are clearly satisfied, indicating the Fe-containing T-,  $\theta'$ - and S-phases are mechanically stable.

#### 3.5 Mechanical and corrosion properties

The hardening response of the two different alloys aged at 180 °C was first analyzed according to the age-hardening curves, as shown in 9a. It is observed that the hardness of the AlCuMgMn and AlCuMgMnFe alloys changes continuously with the time of artificial aging, and both alloys exhibit two age-hardening peaks. The first age-hardening peak of the AlCuMgMn alloy was completed at 26 h with a hardness of 133.9 HV, while the AlCuMgMnFe alloy completed the first age-hardening peak at 20 h with a hardness of 113.5 HV. The second stage of age hardening is relatively slow, with the AlCuMgMn and AlCuMgMnFe alloys reaching peak hardness of 138.6 HV at 88 h and 121.8 HV at 64 h, respectively. In the later stage of aging, the hardness of the AlCuMgMn alloy decreases rapidly, while a relatively slight decrease in the hardness occurs for the AlCuMgMnFe alloy. The microaddition of 0.5 wt% Fe decreases the

aging hardening of the AlCuMgMn alloy.

Fig. 9b shows the engineering stress-strain curves and corresponding property parameters (inset) of the peak-aged AlCuMgMn and AlCuMgMnFe alloys. As can be seen, the yield strength (YS), ultimate tensile strength (UTS) and elongation (EL) of AlCuMgMn alloy at room temperature are 244 MPa, 362 MPa and 11.7%, respectively. The AlCuMgMn alloy with 0.5 wt% Fe addition shows decreased YS (172 MPa) and UTS (335 MPa) but increased EL (14.5%) value than the alloy without Fe addition. The calculation result indicates lower Young's modulus E, bulk modulus B and shear modulus G of main precipitates of Fe-containing  $\theta$ ' than those of pure  $\theta$ ' (Fig. 8), thereby contributing to the reduced strength of AlCuMgMnFe alloy relative to the AlCuMgMn alloy. The increase in EL of AlCuMgMnFe alloy is mainly because the main hardening precipitates of Fe-containing  $\theta'$  show an improved ductility relative to the pure  $\theta'$  phase in AlCuMgMn alloy, as shown in Fig. 8. Another possible reason is that the addition of Fe refines the Al grain size [42], as shown in Fig. 1. Meanwhile, the coarse Al<sub>7</sub>Cu<sub>2</sub>Fe constituents in the peak-aged AlCuMgMnFe alloy are heavily enriched with Cu solute atoms, which impair the precipitation hardening effect due to the considerable solute expenditure. Therefore, it can be concluded that there is an adverse effect of 0.5 wt% Fe on the age hardening and mechanical properties of AlCuMgMn alloy. Similarly, previous works also found that the presence of Fe in Al-Cu alloys is generally reported to have a detrimental effect on the strength and fatigue properties of alloys [11, 34].

In addition, the effect of Fe micro-addition on the tensile fracture morphology of two different peak-aged alloys was studied by SEM observation. Fig. 9c shows that a

large number of dimples are found at the fracture of the AlCuMgMn alloy, indicating the ductile fracture. The AlCuMgMnFe alloy possesses a fracture morphology similar to that of the AlCuMgMn alloy, suggesting the ductile fracture of the alloy, as shown in Fig. 9d. Close observation shows that some second-phase particles exist in the dimples of both alloys, and the size of these second-phase particles is identical in two different alloys. This further demonstrates that the reduced strength and increased ductility of the AlCuMgMnFe alloy are largely related to the primary hardening precipitates of the Fecontaining  $\theta$ .

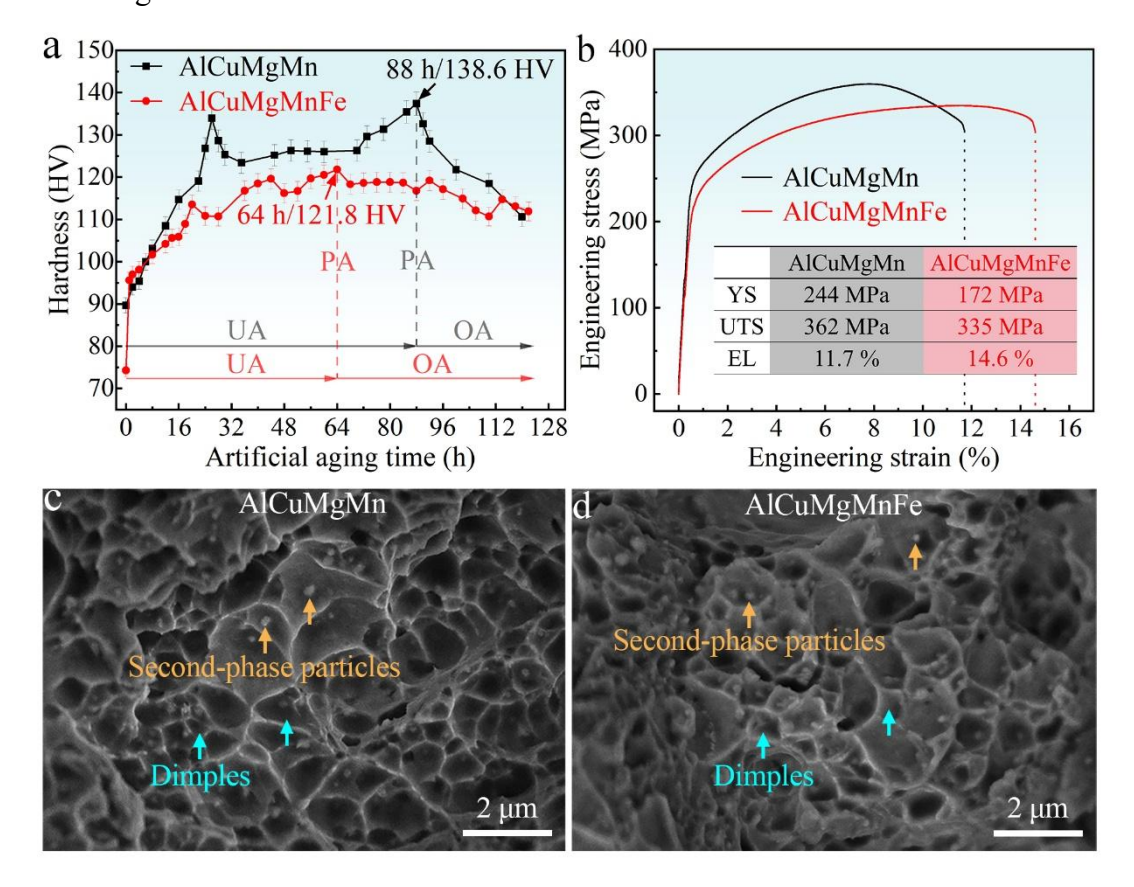


Fig. 9. Age-hardening response, tensile properties and fracture morphology of two different alloys. (a) Age hardening curves at 180 °C. (b) Engineering stress-strain curves of two peak-aged alloys. The corresponding performance parameters are shown in the inset. (c) and (d) Representative fracture morphology of peak-aged AlCuMgMn and

AlCuMgMnFe alloys, respectively. UA, under aging; PA, peak aging; OA, over aging; YS, yield strength, UTS, ultimate tensile strength; EL, elongation.

Intergranular corrosion is an important indicator of corrosion resistance and occurs inward along the boundaries between grains of alloys. The corrosion depth of the cross sections of two peak-aged alloys was examined using an optical microscope (OM), as shown in Figs. 10a and d. The corrosion depth of AlCuMgMn alloy is measured to be 53 µm (Fig. 10a). In comparison, the corrosion depth of AlCuMgMnFe alloy is increased to 97 µm. Therefore, it can be concluded that the addition of Fe element largely lowers the IGC resistance of AlCuMgMn alloy. It is known that the IGC is related to the width of precipitation free zone (PFZ) and grain boundary precipitates (GBPs) of the alloys. For this reason, the PFZ width and GBPs of two peak-aged alloys were characterized by HAADF-STEM, as shown in Figs. 10b and e. The characterization result shows that the peak-aged AlCuMgMn alloy has a PFZ width of ~164 nm, which is smaller than that (~258 nm) of peak-aged AlCuMgMnFe alloy.

In addition, it is found that the peak-aged AlCuMgMn alloy has a discontinuous GBPs distribution. In comparison, the AlCuMgMnFe alloy features consecutive GBPs. The Fe element in the alloy could stabilize the S-phase and θ'-phase precipitates at the grain boundaries, thereby impeding their dissolution and coarsening at the grain boundaries during thermal aging. This results in the increased PFZ width and consecutive GBPs of the peak-aged AlCuMgMnFe alloy relative to AlCuMgMn alloy. The wider PFZ indicates larger corrosion channels [2], contributing to the reduced IGC

property of AlCuMgMnFe alloy. In the meantime, consecutive GBPs increases the corrosion sites between precipitates and the Al matrix around grain boundaries. What is more, increased corrosion potential for the Fe-containing GBPs compared to that of the Fe-free GBPs further accelerates the anodic dissolution of the Al matrix around the Fe-containing GBPs.

Electrochemical corrosion tests were also conducted on two different peak-aged alloys in a 3.5wt% NaCl solution. Fig. 10c shows the time vs. potential curves of two alloys, where one can see that the AlCuMgMnFe alloy has a lower OCP compared to the AlCuMgMn alloy, with OCP values of -0.740 V and -0.734 V, respectively. Generally, the higher the OCP, the better the thermodynamic stability of metals or alloys. Consequently, the minor addition of Fe increases the sensitivity of the AlCuMgMn alloy to electrochemical corrosion. Fig. 10f shows the potentiodynamic polarization curves of two different peak-aged alloys in a 3.5wt% NaCl solution. By fitting the potentiodynamic polarization curves, the corrosion potential  $(E_{corr})$  and corrosion current density  $(I_{corr})$  related to the corrosion property are obtained, as shown in Table 3. The results indicate that the AlCuMgMn alloy delivers an  $E_{\rm corr}$  of -1.375 V and an  $I_{\rm corr}$  of 2.782  $\times$  10<sup>-4</sup> A/cm<sup>2</sup>In comparison, the AlCuMgMnFe alloy has a slightly decreased  $E_{\rm corr}$  of -1.387 V but a larger  $I_{\rm corr}$  of 4.330 × 10<sup>-4</sup> A/cm<sup>2</sup>. Consistent with the change of OCP, the Fe minor addition also induces a decrease in  $E_{corr}$ . This implies an elevated corrosion tendency of the AlCuMgMn alloy due to a minor Fe addition. The higher I<sub>corr</sub> value of the AlCuMgMnFe alloy indicates the faster corrosion rate of the alloy than that of the AlCuMgMn alloy.

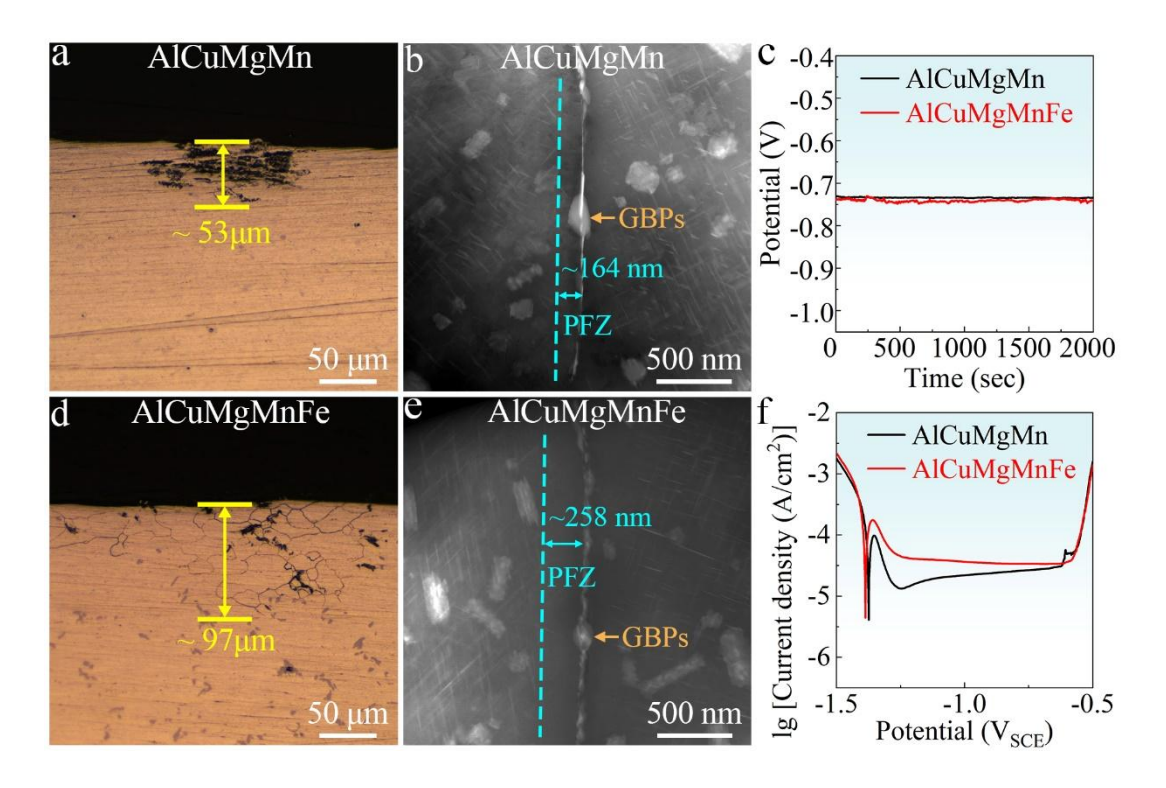


Fig. 10. Comparison of corrosion resistance between two different peak-aged alloys. (a) and (d) Cross-sectional intergranular corrosion of AlCuMgMn and AlCuMgMnFe alloys, respectively by OM. (b) and (e) The PFZ width of AlCuMgMn and AlCuMgMnFe alloys, respectively by HAADF imaging. (c) and (f) The OCP and potentiodynamic polarization curves of two alloys.

Table 3 Parameters for electrochemical corrosion extracted from Fig. 10f

Samples	Aging condition	$E_{\rm corr}$ vs. SCE (V)	$I_{\rm corr}/({\rm A/cm^2})$
AlCuMgMn	Т6	-1.375	2.782×10 <sup>-4</sup>
AlCuMgMnFe	Т6	-1.387	4.330×10 <sup>-4</sup>

#### 4. Conclusions

The micromechanism of 0.5 wt% Fe minor addition-induced property degradation of the Al-5.1Cu-0.65Mg-0.8Mn (wt%) alloy has been studied by atomic scale STEM-HAADF/EDS characterization and first-principles calculations. The main conclusions are summarized as follows: (1) The Fe minor addition to the AlCuMgMn alloy leads to a slight decrease in the size of Al grains and an evident formation of coarse  $Al_7Cu_2Fe$  constituent particles. (2) The T-phase dispersoids,  $\theta$ '- and S-phase precipitates, can accommodate a certain amount of Fe to form Fe-containing second-phase particles. There is a preference for Fe to occupy the Mn and/or Cu sites of the T,  $\theta$ ' and S phases, contributing to an increase in the stiffness of the T and S phases but a decrease in the stiffness of the  $\theta$ ' phase. (3) The  $\theta$ ' is main hardening precipitate in the peak-aged AlCuMgMn and AlCuMgMnFe alloys. Compared with the AlCuMgMn alloy, the degraded tensile strength of the AlCuMgMnFe alloy results from the decreased stiffness of the Fe-containing  $\theta$ ' precipitates. (4) The degraded corrosion resistance of the AlCuMgMnFe alloy is attributed to the increased PFZ width and consecutive GBPs.

# CRediT authorship contribution statement

Xinjian Chen: Methodology, Investigation, Formal analysis, Writing - original draft,
Data curation, Bin Wang: Investigation, Formal analysis, Data curation, Zhen Wang:
Investigation, Formal analysis, Deyu Zhang: Investigation, Formal analysis, Hong
Wang: Investigation, Formal analysis, Jiahai Li: Investigation, Formal analysis, Jin

Wu: Investigation, Formal analysis, Junfen Zhao: Investigation, Formal analysis, Xizhou Kai: Investigation, Formal analysis, Manping Liu: Investigation, Formal analysis, Yutao Zhao: Investigation, Formal analysis, Shihao Wang: Writing - Review & Editing. Shuangbao Wang: Conceptualization, Funding acquisition, Supervision, Project administration, Writing - Review & Editing.

## Data availability

The data supporting the findings of this study are available from the corresponding author on request.

#### **Declaration of competing interest**

The authors declare that they have no known competing financial interests or personal relationships that could have appeared to influence the work reported in this paper.

#### Acknowledgement

The authors appreciate the support from the National Natural Science Foundation of China (Grant Nos. U20A20274, 52061003), the Natural Science Foundation of Yunnan Province (Grant No. 202301AT070209) and the Science and Technology Major Project of Yunnan Province (Grant No. 202102AG050017).

#### References

[1] Raabe D, Tasan CC, Olivetti EA, Strategies for improving the sustainability of structural metals, Nature. 2019;575(7781):64.

- [2] Pan S, Chen XJ, Liao GZ, Ali A, Wang SB, Developing a high-performance Al-Mg-Si-Sn-Sc alloy for essential room-temperature storage after quenching: aging regime design and micromechanisms, Rare Metals. 2023;42(11):3814.
- [3] Zhang X, Chen Y, Hu J, Recent advances in the development of aerospace materials, Progress in Aerospace Sciences. 2018;97:22.
- [4] Lu Q, Wang J, Li H, Jin S, Sha G, Lu J, et al., Synergy of multiple precipitate/matrix interface structures for a heat resistant high-strength Al alloy, Nature Communications. 2023;14(1):2959.
- [5] Lin B, Lou ZH, Fan JL, Zheng CK, Zhang WW, Effect of Fe Content on Microstructures and Mechanical Properties of the Heat-Treated Squeeze Cast Al-5.0Cu-0.6Mn Alloy, Materials Science Forum. 2015;817:82.
- [6] Andersen SJ, Marioara CD, Friis J, Wenner S, Holmestad R, Precipitates in aluminium alloys, Advances in Physics: X. 2018;3(1):1479984.
- [7] Dursun T, Soutis C, Recent developments in advanced aircraft aluminium alloys, Materials & Design (1980-2015). 2014;56:862.
- [8] Wang SC, Starink MJ, Precipitates and intermetallic phases in precipitation hardening Al–Cu–Mg–(Li) based alloys, International Materials Reviews. 2005;50(4):193.
- [9] Shen Z, Liu C, Ding Q, Wang S, Wei X, Chen L, et al., The structure determination of Al<sub>20</sub>Cu<sub>2</sub>Mn<sub>3</sub> by near atomic resolution chemical mapping, Journal of Alloys and Compounds. 2014;601(0):25.
- [10] Zhang JB, Zhang YA, Zhu BH, Liu RQ, Wang F, Liang QM, Characterization of microstructure and mechanical properties of Al–Cu–Mg–Ag–(Mn/Zr) alloy with high Cu:Mg, Materials & Design. 2013;49:311.
- [11] Zhang L, Gao J, Damoah LNW, Robertson DG, Removal of iron from aluminum: A review, Mineral Processing and Extractive Metallurgy Review. 2012;33(2):99.
- [12] Zhao Y, Zhang W, Yang C, Zhang D, Wang Z, Effect of Si on Fe-rich intermetallic formation and mechanical properties of heat-treated Al-Cu-Mn-Fe alloys, Journal of Materials Research. 2018;33(8):898.
- [13] Zhang B, Wang J, Wu B, Oguzie EE, Luo K, Ma XL, Direct observation of atomic-scale origins of local dissolution in Al-Cu-Mg alloys, Scientific Reports. 2016;6(1):39525.
- [14] Wang J, Zhang B, Zhou YT, Ma XL, Multiple twins of a decagonal approximant embedded in S-Al2CuMg phase resulting in pitting initiation of a 2024Al alloy, Acta Materialia. 2015;82:22.
- [15] Bo G-W, Wang G, Jiang F-L, Liu C, Chen R, Zhang H, Dynamic softening and microstructural evolution during hot deformation of Al–Cu–Mg–Zr alloys with different homogenization cooling rates, Rare Metals. 2021;40(3):626.
- [16] Wang SB, Chen JH, Yin MJ, Liu ZR, Yuan DW, Liu JZ, et al., Double-atomic-wall-based dynamic precipitates of the early-stage S-phase in AlCuMg alloys, Acta Materialia. 2012;60(19):6573.
- [17] Pan C, Yang Y, Wang S, Liu Y, Hu S, Wang Z, et al., Atomistic building blocks of one-dimensional Guinier–Preston–Bagaryatsky zones in Al-Cu-Mg alloys, Materials & Design. 2020;187:108393.
- [18] Kovarik L, Mills MJ, Ab initio analysis of Guinier-Preston-Bagaryatsky zone nucleation in Al-Cu-Mg alloys, Acta Materialia. 2012;60(9):3861.
- [19] Han X, Wang S, Wei B, Pan S, Liao G, Li W, et al., Influence of Sc Addition on Precipitation Behavior and Properties of Al-Cu-Mg Alloy, Acta Metallurgica Sinica (English Letters). 2022;35:948.
- [20] Zhou L, Wu CL, Xie P, Niu FJ, Ming WQ, Du K, et al., A hidden precipitation scenario of the  $\theta'$ -phase in Al-Cu alloys, Journal of Materials Science & Technology. 2021;75:126.
- [21] Bourgeois L, Dwyer C, Weyland M, Nie J-F, Muddle BC, Structure and energetics of the coherent

- interface between the  $\theta'$  precipitate phase and aluminium in Al–Cu, Acta Materialia. 2011;59(18):7043.
- [22] Ringer SP, Sofyan BT, Prasad KS, Quan GC, Precipitation reactions in Al–4.0Cu–0.3Mg (wt.%) alloy, Acta Materialia. 2008;56(9):2147.
- [23] Schueller RD, Sachdev AK, Wawner FE, Interfacial structure of the cubic σ phase, Scripta Metallurgica et Materialia. 1992;27(10):1289.
- [24] Gao YH, Cao LF, Kuang J, Song H, Liu G, Zhang JY, et al., Solute repositioning to tune the multiple microalloying effects in an Al–Cu alloy with minor Sc, Fe and Si addition, Materials Science and Engineering: A. 2021;803:140509.
- [25] Zhao Y, He W, Medina J, Song D, Sun Z, Xue Y, et al., Contribution of the Fe-rich phase particles to the high temperature mechanical behaviour of an Al-Cu-Fe alloy, Journal of Alloys and Compounds. 2024;973:172866.
- [26] Egerton RF, Li P, Malac M, Radiation damage in the TEM and SEM, Micron. 2004;35(6):399.
- [27] Kohl H, Reimer L, Transmission electron microscopy: physics of image formation, Springer2008.
- [28] Clark SJ, Segall MD, Pickard CJ, Hasnip PJ, Probert MIJ, Refson K, et al., First principles methods using CASTEP, Zeitschrift fuer Kristallographie. 2005;220:567.
- [29] Wolverton C, Ozoliņš V, First-principles aluminum database: Energetics of binary Al alloys and compounds, Physical Review B. 2006;73(14):144104.
- [30] Wang S, Liu Y, Liu Y, Shi Z, Zhou J, Zhu J, et al., Identifying the surface properties of Ti<sub>3</sub>C<sub>2</sub>T<sub>x</sub> MXene through transmission electron microscopy, Cell Reports Physical Science. 2022;3(11):101151.
- [31] Liu ZK, Zhang H, Ganeshan S, Wang Y, Mathaudhu SN, Computational modeling of effects of alloying elements on elastic coefficients, Scripta Materialia. 2010;63(7):686.
- [32] Ravindran P, Fast L, Korzhavyi PA, Johansson B, Wills J, Eriksson O, Density functional theory for calculation of elastic properties of orthorhombic crystals: Application to TiSi2, Journal of Applied Physics. 1998;84(9):4891.
- [33] Shen Z, Wagoner RH, Clark WAT, Dislocation and grain boundary interactions in metals, Acta Metallurgica. 1988;36(12):3231.
- [34] Gao YH, Kuang J, Liu G, Sun J, Effect of minor Sc and Fe co-addition on the microstructure and mechanical properties of Al-Cu alloys during homogenization treatment, Materials Science and Engineering: A. 2019;746:11.
- [35] Birbilis N, Zhu YM, Kairy SK, Glenn MA, Nie JF, Morton AJ, et al., A closer look at constituent induced localised corrosion in Al-Cu-Mg alloys, Corrosion Science. 2016;113:160.
- [36] Gao M, Feng CR, Wei RP, An analytical electron microscopy study of constituent particles in commercial 7075-T6 and 2024-T3 alloys, Metallurgical and Materials Transactions A. 1998;29(4):1145.
- [37] Tao C, Cheng X-N, Li Z-Q, Liu G-L, Xu F-H, Xie S-K, et al., Mechanism of cryogenic, solid solution and aging compound heat treatment of die-cast Al alloys considering microstructure variation, Rare Metals. 2023;42(9):3130.
- [38] Hughes AE, Parvizi R, Forsyth M, Microstructure and corrosion of AA2024, 2015;33(1-2):1.
- [39] Hughes AE, Glenn AM, Wilson N, Moffatt A, Morton AJ, Buchheit RG, A consistent description of intermetallic particle composition: An analysis of ten batches of AA2024-T3, Surface and Interface Analysis. 2013;45(10):1558.
- [40] Hutchinson CR, Ringer SP, Precipitation processes in Al-Cu-Mg alloys microalloyed with Si, Metallurgical and Materials Transactions A. 2000;31(11):2721.
- [41] Sofyan BT, Raviprasad K, Ringer SP, Effects of microalloying with Cd and Ag on the precipitation process of Al–4Cu–0.3Mg (wt%) alloy at 200°C, Micron. 2001;32(8):851.

- [42] Liao G, Wei B, Pan S, Wang S, Phase structure modification-based property improvement of Al-4.3Cu-1.6Mg-0.2Sc (wt%) alloy, Materials Characterization. 2023;196:112664.
- [43] Geng J, Li Y, Liu G, Xiao H, Hong T, Huang J, et al., Segregation of S precipitates at T/Al interfaces and relevant effects on localized corrosion mechanisms in Al-Cu-Mg alloy, Materials Characterization. 2020;168:110571.
- [44] Sunde JK, Johnstone DN, Wenner S, van Helvoort ATJ, Midgley PA, Holmestad R, Crystallographic relationships of T-/S-phase aggregates in an Al–Cu–Mg–Ag alloy, Acta Materialia. 2019;166:587.
- [45] Chen Y, Zhang Z, Chen Z, Tsalanidis A, Weyland M, Findlay S, et al., The enhanced theta-prime ( $\theta'$ ) precipitation in an Al-Cu alloy with trace Au additions, Acta Materialia. 2017;125:340.
- [46] Sha G, Marceau RKW, Gao X, Muddle BC, Ringer SP, Nanostructure of aluminium alloy 2024: Segregation, clustering and precipitation processes, Acta Materialia. 2011;59(4):1659.
- [47] Liu ZR, Chen JH, Wang SB, Yuan DW, Yin MJ, Wu CL, The structure and the properties of S-phase in AlCuMg alloys, Acta Materialia. 2011;59(19):7396.
- [48] Shang SL, Saengdeejing A, Mei ZG, Kim DE, Zhang H, Ganeshan S, et al., First-principles calculations of pure elements: Equations of state and elastic stiffness constants, Computational Materials Science. 2010;48(4):813.
- [49] Mouhat F, Coudert F-X, Necessary and sufficient elastic stability conditions in various crystal systems, Physical Review B. 2014;90(22):224104.